# Flux penetration into superconducting $Nb_3Sn$ in oblique magnetic fields

Diana G. Gheorghe, Mariela Menghini, and Rinke J. Wijngaarden
*Department of Physics and Astronomy, Faculty of Sciences, Vrije Universiteit, De Boelelaan 1081, 1081 HV Amsterdam, The Netherlands*

Ernst Helmut Brandt
*Max-Plank-Institut für Metallforschung, D-70506 Stuttgart, Germany*

Grigorii P. Mikitik
*B. Verkin Institute for Low Temperature Physics & Engineering, Ukrainian Academy of Sciences, Kharkov 61103, Ukraine*

Wilfried Goldacker
*Forschungszentrum Karlsruhe, Institute of Technical Physics, P.O. Box 3640, 76021 Karlsruhe, Germany*
(Received 7 March 2006; published 14 June 2006)

Penetration of magnetic flux into a rectangular platelet of superconducting $Nb_3Sn$ subject to an oblique magnetic field is studied by magneto-optical imaging. Flux patterns are observed for three distinct scenarios in which the final magnetic field vector is applied differently: (A) the vector has a fixed direction but its magnitude changes from zero to the final value, (B) first the perpendicular component is applied and then the in-plane component, and (C) vice versa. These scenarios lead to distinctly different final states that are consistent with theoretical predictions.

DOI: 10.1103/PhysRevB.73.224512 PACS number(s): 74.25.Dw, 74.25.Qt, 74.25.Sv

## I. INTRODUCTION

The concept of the critical state introduced by Bean[1] is widely used to analyze various properties of the vortex phase in type-II superconductors. For such an analysis, often the simplest solutions of the critical state problem are used, which describe the distribution of magnetic fields and currents in a slab or cylinder with the applied magnetic field parallel to its surface. It has been experimentally shown, however, that the shape of real samples or a misalignment of the external magnetic field with respect to the symmetry axes of the specimen strongly affect the morphology and dynamics of the flux fronts, leading to complicated current distributions inside superconductors, see, e.g., Refs. 2–8. To account for this fact, the concept of the critical state was generalized.[9–13] An interesting result of such extensions is that, even in simple experimental situations, the properties of the critical state may strongly differ from those of cylinders or slabs in parallel applied fields.[13] In particular, this occurs for long superconducting strips in oblique magnetic fields,[14–16] i.e., in many experiments with high-$T_c$ superconductors.

The critical state in a long strip placed in an oblique magnetic field was studied by Zhukov *et al.*[17] for the situation when the magnitude of the applied magnetic field $H_a$ considerably exceeds the field of full-flux penetration into the sample, $H_p$. An attempt to calculate the distribution of currents in superconductors of different geometries subject to tilted magnetic fields with $H_a < H_p$ was made by Karmakar and Bhagwat.[18] In analogy to the critical state problem for a slab or cylinder in parallel magnetic fields, they assumed that with increasing magnitude of the external field the currents change only at the flux fronts and remain constant in areas already penetrated by the magnetic flux. However, the accurate analysis of the critical state problem for superconducting strips in oblique magnetic fields[14–16] revealed that, as the external field is changed, the currents redistribute not only at the flux fronts but also in the already penetrated region. Moreover, depending on the magnetic history, different current distributions are predicted in the strip under the same final experimental conditions. According to Refs. 15 and 16, this difference between the critical states in *thin* strips with thickness $d$ much less than width $2w$ can be detected by measuring the magnetic field profiles on their surface, e.g., by magneto-optical imaging. However, for this difference of the profiles to appear in thin strips, it is necessary that the flux-line pinning in the superconductor is not described by the simple Bean model with constant critical current density $j_c$. A nonconstant $j_c$ occurs, e.g., when columnar defects are introduced into the sample that give rise to *anisotropic* flux-line pinning.[4–7] In the present paper we demonstrate experimentally and theoretically that in *thick* strips (when $d/w$ is not too small) a dependence on the history and an asymmetry of the profiles appears even in the simplest case $j_c$=const, and we show that the calculated magnetic-field profiles and the obtained experimental data are in a good agreement.

In this paper we investigate the dynamics of flux fronts in a homogeneous $Nb_3Sn$ superconducting platelet subject to an oblique magnetic field by means of magneto-optical imaging and by means of simulations according to the ideas of Refs. 14–16. The history-dependence of the flux-front sequence is investigated for three different scenarios of switching on the external field: (A) the external field $H_a(H_{ax},0,H_{az})$ is increased at a fixed ratio $H_{az}/H_{ax}$, (b) the $H_{az}$ component is switched on first, followed by $H_{ax}$, and (c) $H_{ax}$ is switched on first and subsequently $H_{az}$. This paper is organized as follows: Section II is a brief description of the theoretical and simulation methods while Sec. III focuses on the experimental technique and sample preparation. In Sec. IV, the experimental results are presented and discussed in comparison

 

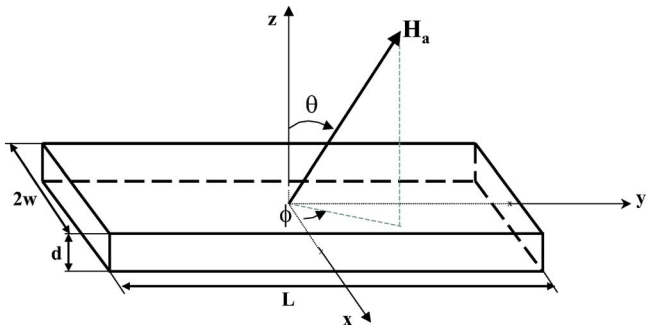


FIG. 1. (Color online) Schematic representation of the experimental geometry. The orientation of the applied vector field $H_a$ with respect to the sample of dimensions $(2w \times L \times d)$ is described by the angles $\theta$ and $\phi$.

with the theoretical results, while in Sec. V, the main conclusions of this work are summarized.

## II. THEORY

Strictly speaking, the critical state problem for a strip in an oblique magnetic field is two-dimensional, and thus the calculation of the local currents and fields is not trivial. Recently it has been shown,[19] however, that for a thin superconductor of width $2w$, length $L$, and thickness $d$ if the condition $d \ll w$, $L$ holds, the problem can be split into two simpler problems: a one-dimensional problem across the thickness of the sample and a problem for the infinitely thin sample, which for long strips is also one-dimensional. This splitting procedure shows that the magnetic field profiles on the flat surfaces of the strip may be expressed[16] as a series in the small parameter $d/w$. The first, main term of the series is a symmetric function with respect to the strip axis, while the second term introduces a small anisotropy of the profiles. This second term differs from zero only if the flux-line pinning is not described by the simple Bean model with constant $j_c$. But when the parameter $d/w$ is not small, such splitting of the critical state problem does not work and one should account for all terms of the above-mentioned series. Therefore for thick strips an asymmetry of the profiles may appear even within the simple Bean model.

To compare our measured flux profiles with theory, we compute the magnetic flux distribution at the surface of a thick strip sample for different scenarios of switching on the externally applied magnetic field: (A) the magnetic field is increased at a fixed angle with respect to the plane of the sample, (B) the perpendicular component of the field $H_{az}$ is switched on first, increased to a certain final value, and then the in-plane component $H_{ax}$ is applied, and (C) is the same approach as in (B) but first $H_{ax}$ and then $H_{az}$ are switched on.

In these calculations we solve the two-dimensional critical state problem numerically by extending the method described in Refs. 20 and 21 to oblique fields. In Refs. 20 and 21 a thick strip in perpendicular magnetic field (along $z$) was considered, which means that the current density $j \| y$ has two symmetry planes, $j(-x,z) = -j(x,z)$ and $j(x,-z) = +j(x,z)$, for strips with rectangular cross section (Fig. 1). When the applied field is tilted in the $x$-$z$ plane, only inversion symmetry survives, $j(-x,-z) = -j(x,z)$. This lower symmetry is the main modification in our theory. We present now the details of this calculation.

Though we are interested here in the solution of the *static* (i.e., ramp-rate independent) critical state model of a thick strip, we obtain this static limit from *dynamic* calculations.[20,21] Namely, we approximate the vortex dynamics in the superconductor by a power-law current-voltage curve and take the limit of large exponent $n \gg 1$. We write the electric field generated by moving vortices in the (isotropic) form

$$\mathbf{E}_v(\mathbf{j},B) = \rho_v(j,B)\mathbf{j}, \tag{1}$$

where $\rho_v(j,B)$ is the resistivity, $j = |\mathbf{j}|$ the current density that drives the vortices, and $B = |\mathbf{B}|$ with $\mathbf{j} \perp \mathbf{B}$ the local magnetic induction or flux density. In the free flux flow limit (zero pinning or very high current density) one has $\rho_v = \rho_{\rm ff} \approx (B/B_{c2})\rho_n$ where $B_{c2}$ is the upper critical field and $\rho_n$ the normal resistivity just above $B_{c2}$. For thermally activated depinning many experiments and theoretical models approximately yield a logarithmic activation energy $U(j) = U_0 \ln(j_c/j)$, which gives

$$E_v = E_c \exp(-U/kT) = E_c \cdot (j/j_c)^n \tag{2}$$

with creep exponent $n = U_0/kT \gg 1$ and (arbitrary) "threshold criterion" $E_c = E(j_c)$ that defines the critical current density $j_c$. The power law (2) in the limit of large $n$ means that at $j < j_c$ one has $E_v = 0$ and the vortices do not move (are pinned), while for $j > j_c$ one has $E_v = \infty$ and the vortices immediately rearrange such that $j$ drops back to $j_c$ everywhere in the superconductor. For large $n = 20-200$, the resulting currents and field profiles only slightly depend on the ramp rate of the applied field: Doubling the ramp rate increases the currents by a factor $2^{1/n} \approx 1 + 0.7/n \approx 1$.

We now derive an equation of motion for the current density $j_y(x,z)$ (which we now denote by $j$) in a long strip filling the volume $|x| \leq w$, $|y| \leq L/2$, $|z| \leq d/2$, with $d < w \ll L$, exposed to an applied magnetic field $\mathbf{H}_a(t) = (H_{ax}, H_{az}) = \mu_0^{-1} \nabla \times \mathbf{A}_a$, where $\mathbf{A}_a = A_a(x,z,t)\hat{\mathbf{y}}$ is the applied vector potential. In the general case, with $\mathbf{r} = (x,y,z)$, the vector potential $\mathbf{A_j}(\mathbf{r})$ caused by the current density $\mathbf{j}(\mathbf{r}) = -\mu_0^{-1}\nabla^2 \mathbf{A_j}$ in the Coulomb gauge $\nabla \cdot \mathbf{A} = 0$ is given by

$$\mathbf{A_j}(\mathbf{r}) = \mu_0 \int d^3r' \frac{\mathbf{j}(\mathbf{r}')}{4\pi|\mathbf{r} - \mathbf{r}'|}, \tag{3}$$

with the integral taken over the volume where the current flows. For our long strip both $\mathbf{j} = j(x,z)\hat{\mathbf{y}}$ and $\mathbf{A_j} = A_j(x,z)\hat{\mathbf{y}}$ are directed along $y$. Integrating Eq. (3) over $y'$ and writing from now on $\mathbf{r} = (x,z)$ we obtain

$$A_j(\mathbf{r}) = \mu_0 \int d^2r' Q(\mathbf{r},\mathbf{r}') j(\mathbf{r}') \tag{4}$$

with the 2D integral kernel

$$Q(\mathbf{r},\mathbf{r}') = \frac{1}{2\pi}\,\mathrm{asinh}\,\frac{L/2}{|\mathbf{r}-\mathbf{r}'|} \approx \frac{1}{2\pi}\ln\frac{L}{|\mathbf{r}-\mathbf{r}'|}. \quad (5)$$

The integral in Eq. (4) is over the rectangular strip cross section, $-w \leqslant x \leqslant w$ and $-d/2 \leqslant z \leqslant d/2$, but actually Eq. (4) applies to strips with cross sections of any shape. If the current distribution is symmetric the integration (4) may be restricted to one-quarter or one-half of the rectangular cross section. In particular for our strip in tilted field $(H_{ax}, H_{az})$, with $j(-x,-z) = -j(x,z)$ we may write

$$A_j(x,z) = \mu_0 \int_{-w}^{w} dx' \int_0^{d/2} dz'\, \widetilde{Q}(x,z;x',z')\, j(x',z') \quad (6)$$

with the inversion-symmetric kernel

$$\widetilde{Q}(x,z;x',z') = \frac{1}{4\pi}\ln\frac{(x+x')^2+(z+z')^2}{(x-x')^2+(z-z')^2}. \quad (7)$$

Note that the strip length $L$ has dropped out here.

To obtain an explicit dynamic equation for the current density $j(x,z,t)$ one has to incorporate the applied vector potential $\mathbf{A}_a$, which for the strip may be chosen along $y$, $\mathbf{A}_a = A_a(x,z,t)\hat{\mathbf{y}}$, $A_a = \mu_0 H_{az} x - \mu_0 H_{ax} z$. Writing the total vector potential as $A = A_j + A_a$ we obtain from Eq. (4),

$$\mu_0 \int d^2r'\, Q(\mathbf{r},\mathbf{r}')\, j(\mathbf{r}',t) = A_j(\mathbf{r},t) = A - A_a. \quad (8)$$

For our strip the induction law $\dot{\mathbf{B}} = -\nabla \times \mathbf{E}$ means $-\dot{A} = E = E_v(j) = E_c \cdot (j/j_c)^n \mathrm{sign}(j)$. Inserting this into the time derivative of Eq. (8) we obtain

$$\mu_0 \int d^2r'\, Q(\mathbf{r},\mathbf{r}')\frac{\partial j(\mathbf{r}',t)}{\partial t} = -E_v(\mathbf{r},t) - \dot{A}_a(\mathbf{r},t). \quad (9)$$

The time derivative of $j$ in Eq. (9) may be moved out from the integral by introducing the inverse integral kernel $K(\mathbf{r},\mathbf{r}') = Q(\mathbf{r},\mathbf{r}')^{-1}$, or the symmetric kernel[20] $\widetilde{K}(\mathbf{r},\mathbf{r}') = \widetilde{Q}(\mathbf{r},\mathbf{r}')^{-1}$, defined by

$$\int d^2r''\, \widetilde{K}(\mathbf{r},\mathbf{r}'')\widetilde{Q}(\mathbf{r}'',\mathbf{r}') = \delta_2(\mathbf{r}-\mathbf{r}'), \quad (10)$$

where $\delta_2(\mathbf{r}) = \delta(x)\delta(z)$ is the 2D delta function. This yields the equation of motion for $j(x,z,t)$,

$$\frac{\partial j(\mathbf{r},t)}{\partial t} = -\mu_0^{-1} \int d^2r'\, \widetilde{K}(\mathbf{r},\mathbf{r}')[E_v(j) + \dot{A}_a(\mathbf{r}',t)] \quad (11)$$

with $E_v(j) = E_v[j(\mathbf{r}',t)]$ and $\dot{A}_a(\mathbf{r}',t) = x'\mu_0 \dot{H}_{az}(t) - z'\mu_0 \dot{H}_{ax}(t)$.

The inverse kernel $\widetilde{K}(\mathbf{r},\mathbf{r}')$ may be computed by a matrix inversion as follows. First, a spatial grid $\mathbf{r}_i = (x_i, z_i)$ is chosen with appropriate weights $w_i$ such that the integrals of any function $f(\mathbf{r})$ over one-half strip cross section $(-w \leqslant x \leqslant w,\ 0 \leqslant z \leqslant d/2)$ are well-approximated by a sum,

$$\int d^2r f(\mathbf{r}) \approx \sum_i f(\mathbf{r}_i) w_i. \quad (12)$$

Then we express the definition (10) by such a sum,

$$\sum_i \widetilde{K}_{li}\widetilde{Q}_{ij} w_i = \delta_{lj}, \quad (13)$$

where $Q_{ij} = Q(\mathbf{r}_i, \mathbf{r}_j)$ and $\delta_{ij}$ equals 1 if $i=j$ and 0 else. The diverging diagonal terms $Q_{ii}$ have to be chosen finite as discussed in Ref. 20. The solution of Eq. (13) is the inverse matrix

$$\widetilde{K}_{ij} = (\widetilde{Q}_{ij} w_i)^{-1}. \quad (14)$$

The accuracy of this method is considerably increased by choosing a nonequidistant grid with narrow spacing near the specimen surface and by taking appropriate diagonal terms $\widetilde{Q}_{ii}$. The equation of motion (11) for $\mathbf{j}(\mathbf{r},t)$ in discrete form reads

$$\frac{\partial j_i(t)}{\partial t} = -\mu_0^{-1} \sum_j \widetilde{K}_{ij}\{E_v[j_j(t)] + \dot{A}_{aj}(t)\}, \quad (15)$$

where the vectors $j_i(t) = j(\mathbf{r}_i, t)$ and $\dot{A}_{ai}(t) = \dot{A}_a(\mathbf{r}_i, t) = x_i \mu_0 \dot{H}_{az}(t) - z_i \mu_0 \dot{H}_{ax}(t)$ are functions of the time $t$. The matrix $K_{ij}$, Eq. (14), is independent of time and has to be computed *only once* for a given geometry. Equation (15) is easily integrated over time $t$ starting with $j_i(t=0) = 0$ and then switching on the applied field $H_a$.

From the resulting current density the magnetic induction follows as $\mathbf{B}(x,z,t) = \nabla \times \mathbf{A} = \mu_0 \mathbf{H}_a(t) + \nabla \times \hat{\mathbf{y}} A_j(x,z,t)$ with $A_j$ from Eq. (6). We compute $\mathbf{B}_i = \mathbf{B}(x_i, z_i)$ by taking the numerical derivatives of $A(x_i, z_i)$ given by

$$A(\mathbf{r}_i,t) = A_a(\mathbf{r}_i,t) + \sum_j \widetilde{Q}_{ij} w_j j_j(t). \quad (16)$$

This method is much more accurate than the direct computation of $\mathbf{B}$ from the current density $j$ by the usual Biot-Savart kernel that is highly singular, containing terms $\propto (\mathbf{r}_i - \mathbf{r}_j)/|\mathbf{r}_i - \mathbf{r}_j|^2$. By putting $z = d/2$ one obtains the magnetic field profiles at the upper surface of the strip that are measured by magneto-optics.

Finally, the magnetic moment per unit length of the strip, $\mathbf{m}(t) = (m_x, m_z)$, is obtained as an integral or sum over the half strip cross section,

$$\mathbf{m}(t) = 2\int_{-w}^{w} dx \int_0^{d/2} dz\, (\hat{\mathbf{x}} z - \hat{\mathbf{z}} x) j(x,z,t)$$
$$\approx 2\sum_i (\hat{\mathbf{x}} z_i - \hat{\mathbf{z}} x_i) j_i(t) w_i. \quad (17)$$

The contributions to $\mathbf{m}(t)$ of the U-turns of the currents at the strip ends (integrals over the $x$ and $z$ components of $\mathbf{j}$, amounting to exactly $\frac{1}{2}\mathbf{m}$) are already considered in Eq. (17).

## III. SAMPLE AND EXPERIMENTAL PROCEDURE

The experiments discussed in this paper have been performed by magneto-optical imaging,[22–24] a spatial and tem-

poral resolved technique that allows direct visualization of the perpendicular component of the local magnetic field, at the surface of a superconducting material. The technique is based on the Faraday effect. For our experiments we used the Faraday effect of a EuSe film[22] with a saturation field of 1 T.

The experiments were carried out on a $Nb_3Sn$ platelet with the following geometrical characteristics: width $2w=0.75$ mm, length $L=2.2$ mm, and thickness $d=175$ $\mu$m. The critical temperature of the material is $T_c=18$ K. The sample was prepared[25] from thoroughly mixed powders of Nb (99.9% purity, deoxidized, mean particle size 35–45 $\mu$m) and Sn (99.5% purity, $<40$ $\mu$m particle size). The stoichiometric composition was chosen with a slight excess of Sn (25.4%), close to the A15 phase boundary. An amount of 700 g powder was put into a stainless steel container internally clad by a Ta foil, which was closed under vacuum by electron beam welding. The powder was precompacted by pressing to a density of 70% of the theoretical value. The container was processed under HIP (hot isostatic pressing) conditions, $T=1100$ °C, P(Ar)=100 MPa for 24 h followed by slow cooling at 150 K/h. The sample was cut out of the container mechanically. The small width $\Delta T_c=0.3$ to 0.4 K of the specific heat transition indicates an excellent sample homogeneity.[25]

A schematic representation of the geometry of the experiment is depicted in Fig. 1, where $\theta$ is the angle between the direction of the applied magnetic field $H_a$ and the $z$ axis perpendicular to the plane of the sample, while $\phi$ defines the angle between the projection of $H_a$ on the plane of the sample and the $x$ axis. The sample was placed inside a commercial Oxford Instruments vector magnet and the magnetic field distribution at its surface was mapped using our magneto-optical image lock-in[23,24] (MO-ILIA) yielding quantitative values for the $z$ component of the magnetic field. The value of the magnetic fields that can be generated by the magnet range between −7 and 7 T along the $z$ axis, i.e., perpendicular to the sample plane, and −1 and 1 T along the $x$ and $y$ axes. By simultaneous use of the superconducting coils, any field orientation with respect to the plane of the sample can be obtained (up to 1 T).

In all experiments, the initial state was prepared the same way, namely by zero-field cooling below the critical temperature to 7 K and $\phi$ was always zero, i.e., the in-plane component of the field is always parallel to the $x$ axis.

## IV. RESULTS AND DISCUSSION

Magneto-optical imaging allows the direct visualization of the magnetic field distribution $H_z(x,y)$ at the surface of a superconductor with high spatial and temporal resolution. From $H_z$, by using an inversion scheme,[26–28] the current and electric field distributions in the superconductor can be determined.

However, it was shown[29] that for an accurate quantitative determination of $H_z(x,y)$ the influence of the in-plane component of the field on the sensitivity of the indicator must be taken into account. For symmetric field configurations the experimental data may be corrected by incorporating approximated $H_x$ values in the inversion scheme[29] or by iteratively solving the Biot-Savart equation and its inverse, in which an in-plane $H_x$ field component contribution is incorporated until convergence is achieved.[30]

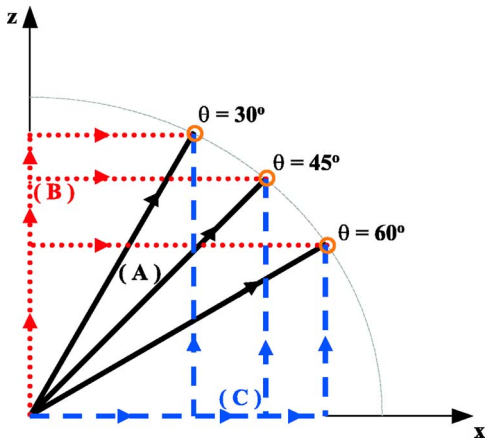


FIG. 2. (Color online) Schematic representation of the possible paths: A (—), B (···), and C (- - -) that can be taken to reach the same applied field $H_a$ (indicated by the orange circle), characterized by the same magnitude of the external field and the same tilt angle $\theta$ (for all scenarios $\phi=0$). We present results for three angles $\theta$ as indicated.

In our more general experimental configuration this correction method encounters difficulties. Instead, to compare experiment and simulation, we calculate an effective "experimental field" $H_z^{\varphi}$ from the simulated $H_z$ and $H_x$ components, as detailed below in Sec. IV A. In Sec. IV B a direct comparison between the simulation data and the experimental results is presented for three scenarios of switching on the external magnetic fields: (A) the magnetic field is increased at a fixed angle $\theta$ with respect to the plane of the sample, (B) $H_z$ is switched on first, increased to a certain value, and then $H_x$ is applied, and (C) the same approach as in (B) only the order of switching on the field components is reversed. A schematic representation of these three possible scenarios is shown in Fig. 2 for three cases: $\theta=30°$, 45°, and 60°.

### A. Calculating the "experimental field" from simulation data

As discussed above, the Faraday angle $\varphi(H_x,H_z)$ that is measured magneto-optically in our experiments is a function of mainly the perpendicular field component $H_z$, but is also influenced by the in-plane field $H_x$. However, a good estimate (with less than 30% error) can be obtained by ignoring the influence of $H_x$. Specifically, we present our magneto-optical results in terms of a "measured" perpendicular field $H_z^{\varphi}=f(\varphi)$, where $f^{-1}(x)=\varphi(0,H_z)$ is determined from a separate experiment, see below.

To compare experiment and simulation, we also express the results of the simulation in terms of $H_z^{\varphi}$ values. These are determined by first finding the Faraday angle $\varphi$ for the simulated values of $H_x$, $H_z$ and then calculating $H_z^{\varphi}$ from that $\varphi$. Specifically, for the simulation, we calculate $H_z^{\varphi}=f(\varphi(H_x,H_z))$ with $H_x$, $H_z$ the results from the simulation.

Of course, for both these procedures, we must know the function $\varphi(H_x,H_z)$. This was determined in a separate ex-

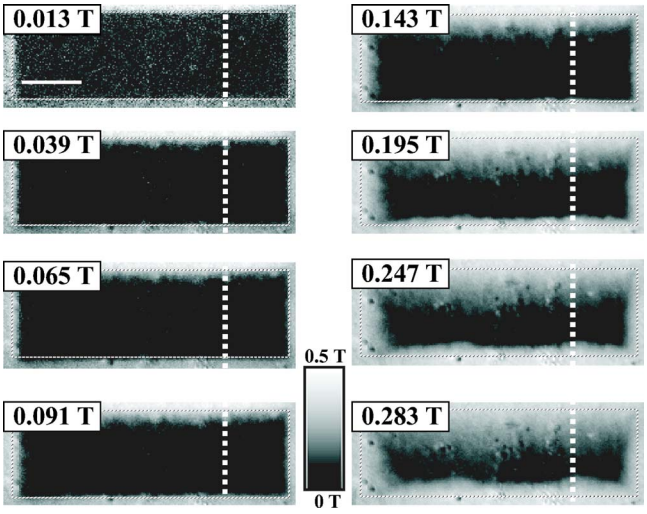


FIG. 3. (Color online) Magneto-optical images for increasing magnitude of the external field (as indicated) in the $Nb_3Sn$ sample. Black indicates zero magnetic field and white indicates high magnetic fields. The edges of the sample are highlighted by the rectangular dashed contour. The external magnetic field was applied at an angle $\theta=45°$ with respect to the plane of the sample (corresponding to the plane of the paper); its projection is parallel to the short edge of the sample. The scale bar in the first image corresponds to 0.5 mm.

periment, without the sample, on the same EuSe indicator and at the same temperature, namely $T=7$ K. For fixed values of the in-plane field component $H_{ax}$ in the interval $[0,0.3]$ T, $H_{az}$ was increased from 0 to 0.3 T in steps of 10 mT. The experimentally obtained values of $\varphi$ on this grid of field values were well-fitted by a function of the form: $\varphi(H_{ax},H_{az})=a_1+a_2H_{ax}+a_3H_{az}+a_4H_{ax}^2+a_5H_{az}^2+a_6H_{ax}H_{az}$, from which the inverse function $f$ as defined above is found analytically.

For comparing experiment and simulation, we used for the critical current density the value $j_c=6.1\times10^9$ A/m$^2$, as calculated from the magnetic field profile of the sample in the critical state, using the inversion algorithm described in Refs. 27 and 28.

Using this calibration and the scheme just discussed, a very nice quantitative agreement between the measured data and the results from the simulation was obtained, as we show in the following section.

### B. Experimental versus simulation results

#### *1. Scenario (A): Magnetic field increased at constant angle*

After zero-field cooling, a magnetic field was applied to the sample under a fixed angle $\theta$ and increased up to 0.507 T in steps of 0.013 T. Magneto-optical images of the sample were taken after each stepwise increase in the magnitude of the external magnetic field.

In Fig. 3 a selection of images showing the evolution of $H_z^{\varphi}$ at the surface of the sample, during an experiment in which $\theta=45°$, is shown. Already at an amplitude of 0.039 T vortices start to nucleate at the upper edge of the sample. However, at the bottom edge no nucleation is observed before the magnetic field reaches 0.091 T. The roughness of the flux fronts is due to static disorder and intrinsic roughening.[31] In nice agreement with the theoretical predictions of Refs. 14–16, the flux fronts at the surface are not symmetric with respect to the center of the superconducting plate.

This is most clearly seen from profiles of the magnetic field, e.g., along the dotted white lines in Fig. 3. Such profiles were determined to examine the influence of the tilt angle $\theta$ on the asymmetry of the flux-front profiles. The results are presented in the left column of Fig. 4. For the case $\theta=0°$ the flux fronts enter the superconductor symmetrically from the upper and lower edges of the sample. For increasing tilt angles $\theta$, the penetration becomes more and more asymmetric. Another interesting feature is that after the flux fronts from opposite edges of the sample meet, the asymmetry decreases.

We compare our experimental findings with calculated profiles at the surface of the sample, for a sample with the same aspect-ratio $d/w$ as the superconducting specimen used in our experiments, namely $d/w=0.47$. The theoretical profiles were calculated using the algorithm of Sec. II and are presented using the procedure described in Sec. IV A. Profiles are shown at each stepwise increase of 0.026 T in the external field $H_a$. The results are shown in the right column of Fig. 4. A very good agreement between the experimental and the simulation findings is observed.

#### *2. Scenario (B): $H_{az}$ first, $H_{ax}$ last*

In this section, as an example for scenario B, we present results for an experiment in which the final state with $\theta=60°$ was reached by first increasing the $H_{az}$ component of the field and afterwards the $H_{ax}$ component.

After zero-field cooling the $Nb_3Sn$ platelet, an external field perpendicular to the plate was applied and increased up to 0.130 T in steps of 0.013 T. The evolution of the experimental profiles at the surface of the sample, with increasing magnitudes of the applied magnetic field, is shown in Fig. 5(a), below the thick curve. As expected, a symmetric evolution of the flux fronts towards the center of the sample is observed. However, as soon as $H_{ax}$ is applied from the thick curve upwards, in steps of 0.013 T up to 0.234 T, the profiles evolve towards an asymmetric state as an in-plane magnetic moment is induced. The magnitude of the in-plane magnetic moment is proportional to $H_{ax}$ and can be observed by the increasing height difference of the profiles at the edges of the sample. The asymmetry of the profiles relative to the center of the superconductor is enhanced for higher in-plane components of the field. The last profile in Fig. 5 corresponds to a total magnetic field vector $H_a=0.27$ T and a tilt angle $\theta=60°$.

The corresponding simulated profiles are shown in Fig. 5(b). Like for scenario A, the theoretical profiles were calculated using the algorithm of Sec. II and are presented using the procedure described in Sec. IV A. Each field profile corresponds to a step increase in the external field of 0.026 T up to $H_a=0.27$ T. A very nice agreement between experiment and simulation can be observed.

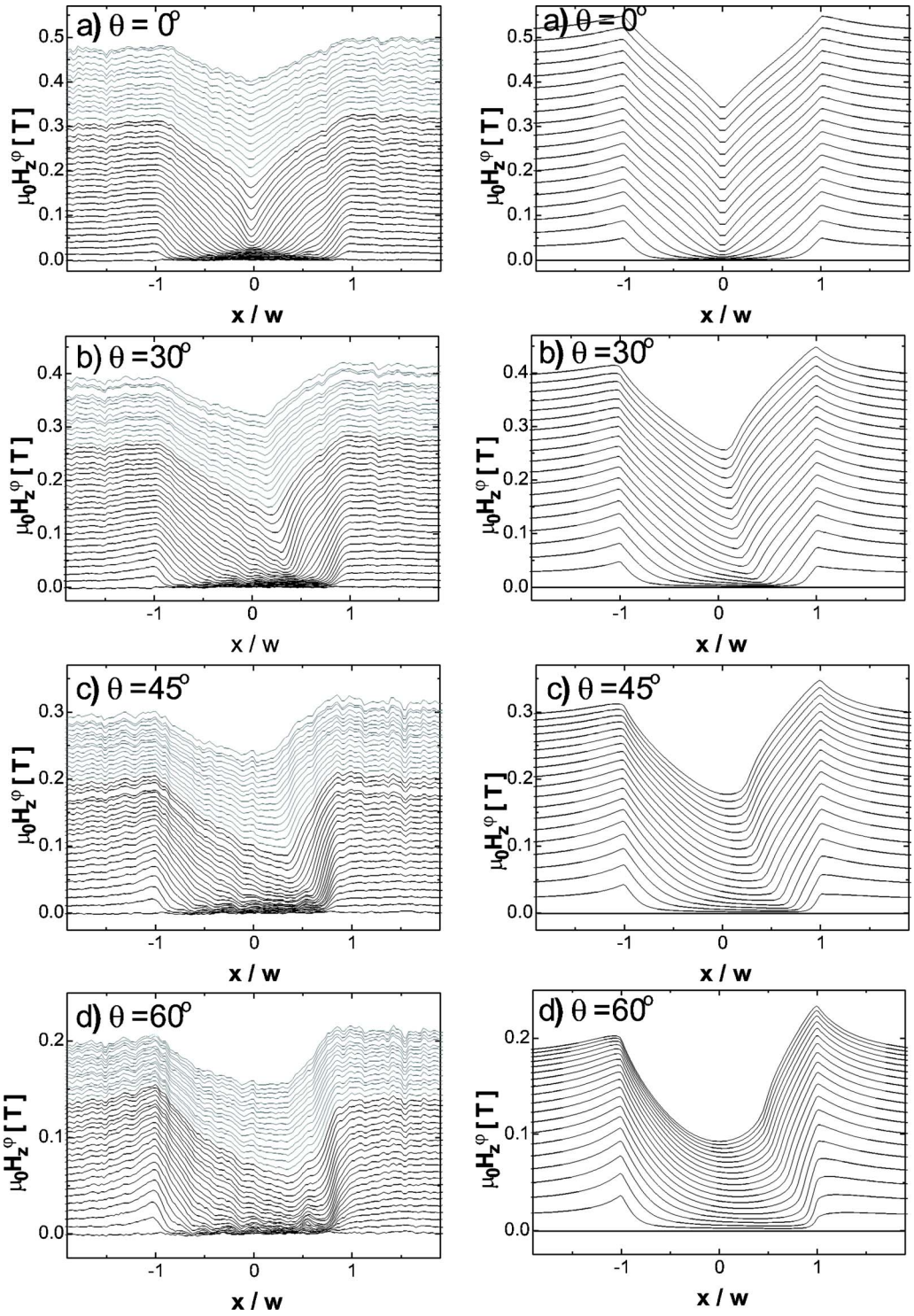


FIG. 4. (Color online) Experimental (left column) and simulated (right column) magnetic field $H_z^{\varphi}$ profiles for scenario A at the surface of the sample for different tilt angles $\theta$ (as indicated). For the experiment the external magnetic field $H_a$ was increased from 0 to 0.507 T in steps of 0.013 T, for the simulation $H_a$ was increased from 0 to 0.507 T in steps of 0.026 T.

#### *3. Scenario (C): $H_{ax}$ first, $H_{az}$ last*

As an example for scenario C we discuss an experiment in which the final state at $\theta$=30° was reached by switching on the $H_{ax}$ component of the magnetic field first (up to 0.13 T in steps of 0.013 T), followed by $H_{az}$ (increased to 0.234 T in steps of 0.013 T).

The evolution of the magnetic flux profile for this scenario is shown in Fig. 6(a). From the first profiles, when only the in-plane magnetic field is applied (below the thick line), it is observed that $H_{ax}$ induces an in-plane magnetic moment. This is evident in the positive and negative peaks at the edges of the sample. The magnitude of this moment reduces

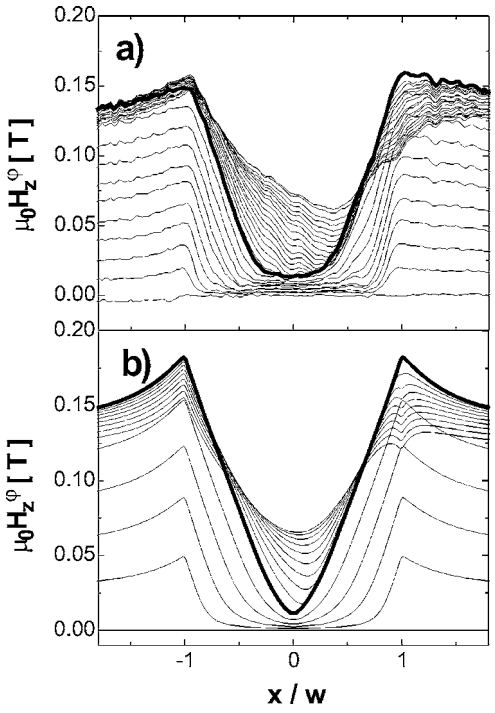


FIG. 5. Magnetic field $H_z^{\varphi}$ profiles for $\theta=60°$, scenario B: (a) experiment and (b) simulation. For the experiment $H_{az}$ was increased first from 0 to 0.130 T in steps of 0.013 T, followed by $H_{ax}$ in steps of 0.013 T, from 0 to 0.234 T. For the simulation $H_{az}$ was increased first from 0 to 0.130 T in steps of 0.026 T, followed by $H_{ax}$ in steps of 0.026 T, from 0 to 0.234 T.

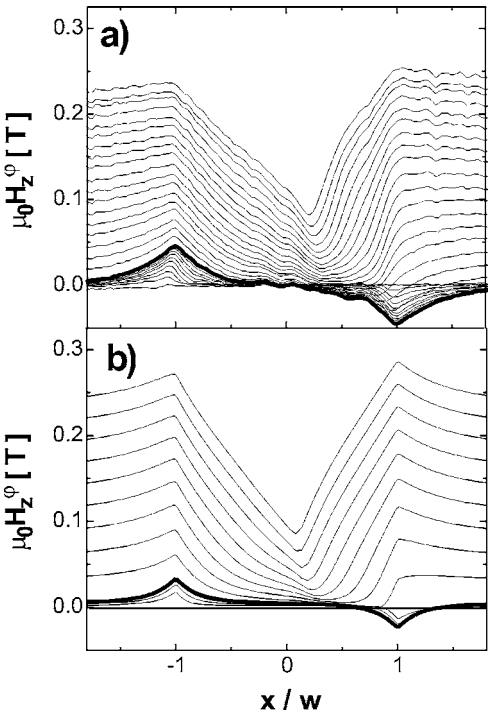


FIG. 6. Evolution of the magnetic field $H_z^{\varphi}$ profile for $\theta=30°$, scenario C: (a) experiment and (b) simulation. For the experiment $H_{ax}$ was increased first from 0 to 0.130 T in steps of 0.013 T, followed by $H_{az}$ in steps of 0.013 T, from 0 to 0.234 T. For the simulation $H_{ax}$ was increased first from 0 to 0.130 T in steps of 0.026 T, followed by $H_{az}$ in steps of 0.026 T, from 0 to 0.234 T.

with increasing magnitude of $H_{az}$ (from the thick black curve upwards). Furthermore, the asymmetry of the flux fronts relative to the center of the superconductor is reduced as $H_{az}$ is increased. The last profile in Fig. 6 corresponds to a total magnetic field vector $H_a=0.27$ T at a tilt angle $\theta=30°$.

The corresponding simulated profiles are shown in Fig. 6(b). Each field profile corresponds to a stepwise increase in the external field up to $H_a=0.27$ T in steps of 0.026 T. Again, a nice agreement between the experimental and the simulated data, calculated using the algorithm of Sec. II and presented using the procedure described in Sec. IV A, is observed.

#### *4. Final states compared*

To determine how the asymmetry of the profiles depends on the scenario (A, B, or C), we show in Fig. 7 the profiles for the same final field $H_a=0.27$ T at $\theta=30°$, 45°, and 60°. The experimental results are shown in the left column in Fig. 7. It is observed that for all the considered cases, the magnetic field profiles are asymmetric with respect to the center of the sample. This asymmetry is related to the in-plane component of the magnetic field $H_x$. Although the applied external field $H_a$ has the same magnitude and tilt angle $\theta$ in all these cases, the final magnetization states are clearly different.

Instead of defining an asymmetry parameter from, e.g., the moments of the profiles, we merely point out that the influence of the in-plane field (as seen from the asymmetry between the sample edges) is largest for scenario B and smallest for scenario C. The observed order BAC can be qualitatively explained as follows: the asymmetry is mainly due to a finite and nonuniform in-plane moment per unit length[16] $M_x(x)=\int_{-d/2}^{d/2} z j_y dz$. When $H_{ax}$ is applied before $H_{az}$ (scenario C), the increase of $H_{az}$ leads to a redistribution of the currents over the thickness of the sample and decreases $M_x$ which was generated by $H_{ax}$. On the other hand, in scenario B, the increase of $H_{ax}$ applied after $H_{az}$ increases $M_x$; and in this case $M_x$ can essentially exceed the value it has in scenario C if the fields $H_{ax}$ and $H_{az}$ are of the order of the field of full flux penetration. Scenario A in which $H_{ax}$ and $H_{az}$ are applied simultaneously is intermediate.

## V. CONCLUSIONS

We have shown by magneto-optical measurements and simulation that if a tilted magnetic field is applied to a superconductor, an asymmetry in flux penetration is observed, in good agreement with the theoretical predictions of Refs. 14–16. This asymmetry is enhanced for larger tilt angles $\theta$. The same final state in the phase diagram, characterized by the same external magnetic field $H_a(H_{ax},H_{az})$ and the same tilt angle can be reached by three different paths: (a) increasing the field at a constant angle, (b) switching on first $H_{az}$ and then $H_{ax}$, or (c) switching on $H_{ax}$ and subsequently $H_{az}$. These different paths lead to a final state in which the magnetization of the sample and the magnetic field profiles at its

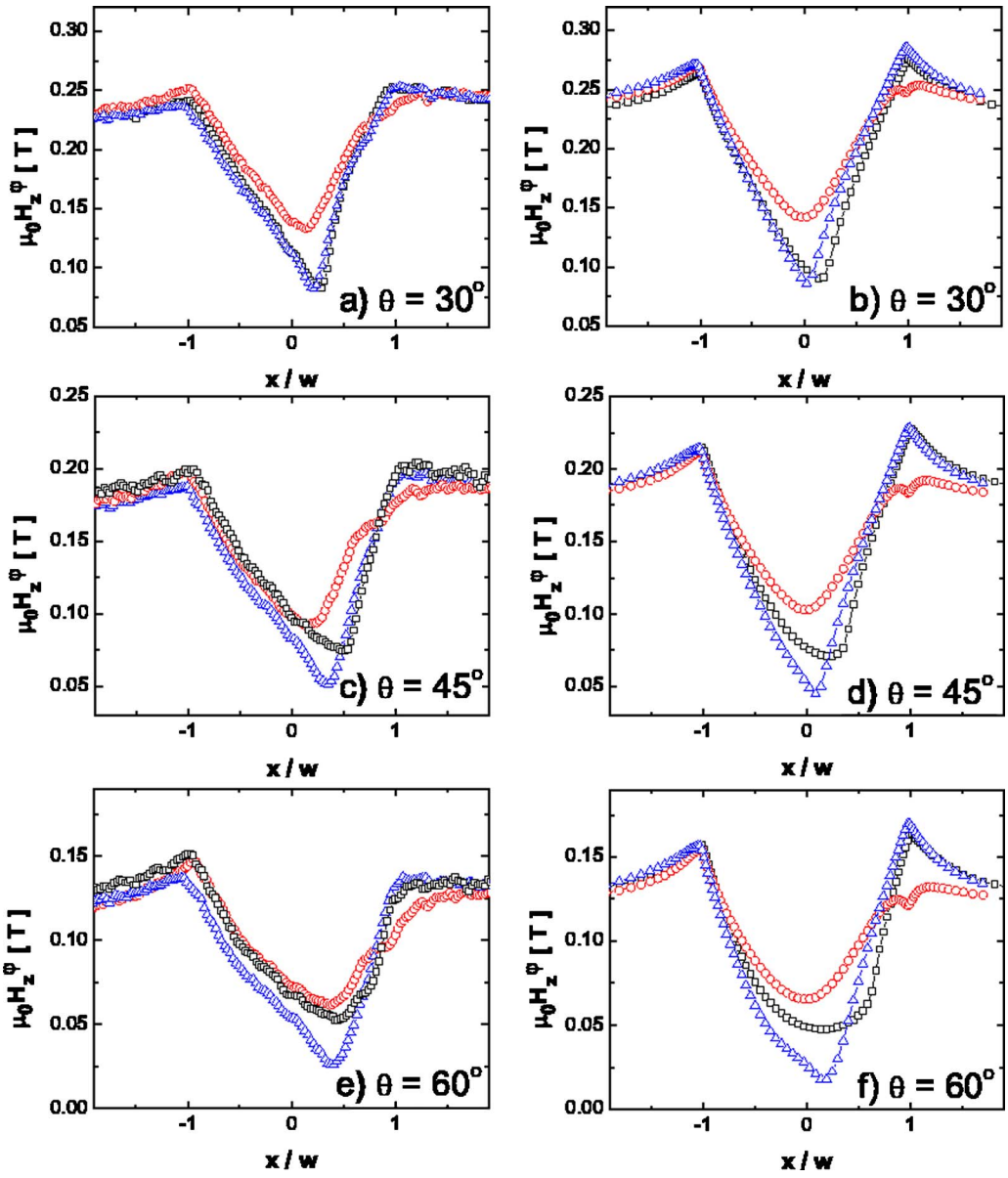


FIG. 7. (Color online) Profiles $H_z^{\varphi}$ from experiment (left column) and simulation (right column) for scenario A (□), B (○), and C (△), all for the same magnitude of the applied field $H_a$=0.27 T at the indicated tilt angles $\theta$.

surface are different. These experimental results agree quantitatively with numerical simulations that were done according to the theoretical ideas of Refs. 14–16 and thus validate these ideas experimentally. A comparison of the scenarios described above reveals that the asymmetry of the flux penetration is the highest when the $x$ component of external field is applied last [scenario (B)] while the most symmetric flux patterns are obtained for scenario (C). Thus we conclude that the observed asymmetry in the magnetic field profiles depends on the history of the superconductor and is related to the remaining strength of the in-plane component $M_x$ of the magnetization.

## ACKNOWLEDGMENTS

This work was supported by FOM (Stichting voor Fundamenteel Onderzoek der Materie) which is financially supported by NWO (Nederlandse Organisatie voor Wetenschappelijk Onderzoek), by the ESF "VORTEX" program, and by the German Israeli Research Grant Agreement (GIF) No. G-705-50.14/01.

[1] C. P. Bean, Rev. Mod. Phys. **36**, 31 (1964).
[2] R. P. Huebener, V. A. Rowe, and R. T. Kampwirth, J. Appl. Phys. **41**, 2963 (1970); T. Schuster, H. Kuhn, E. H. Brandt, M. V. Indenbom, M. Kläser, G. Müller-Vogt, H.-U. Habermeier, H. Kronmüller, and A Forkl, Phys. Rev. B **52**, 10375 (1995).
[3] S. Gotoh and N. Koshizuka, Physica C **176**, 300 (1991).
[4] Th. Schuster, M. V. Indenbom, H. Kuhn, H. Kronmüller, M. Leghissa, and G. Kreiselmeyer, Phys. Rev. B **50**, 9499 (1994).
[5] Th. Schuster, M. V. Indenbom, H. Kuhn, E. H. Brandt, and M. Konczykowski, Phys. Rev. Lett. **73**, 1424 (1994).
[6] Th. Schuster, H. Kuhn, and E. H. Brandt, Phys. Rev. B **54**, 3514 (1996).
[7] M. A. Avila, L. Civale, A. V. Silhanek, R. A. Ribeiro, O. F. de Lima, and H. Lanza, Phys. Rev. B **64**, 144502 (2001).
[8] M. V. Indenbom, A. Forkl, B. Ludescher, H. Kronmüller, H.-U. Habermeier, B. Leibold, G. D'Anna, T. W. Li, P. H. Kes, and A. A. Menovsky, Physica C **226**, 325 (1994); G. P. Mikitik, E. H. Brandt, and M. Indenbom, Phys. Rev. B **70**, 014520 (2004).
[9] C. P. Bean, J. Appl. Phys. **41**, 2484 (1970).
[10] J. R. Clem, Phys. Rev. B **26**, 2463 (1982).
[11] I. V. Voloshin, A. V. Kalinov, S. E. Savel'ev, L. M. Fisher, V. A. Yampolskii, and F. Perez-Rodrigues, JETP **84**, 592 (1997).
[12] A. Badia and C. López, Phys. Rev. B **65**, 104514 (2002).
[13] G. P. Mikitik and E. H. Brandt, Phys. Rev. B **71**, 012510 (2005).
[14] G. P. Mikitik, E. H. Brandt, and M. Indenbom, Phys. Rev. B **70**, 014520 (2004).
[15] E. H. Brandt and G. P. Mikitik, Phys. Rev. B **72**, 024516 (2005).
[16] G. P. Mikitik and E. H. Brandt, Phys. Rev. B **72**, 064506 (2005).
[17] A. A. Zhukov, G. K. Perkins, Yu. V. Bugoslavsky, and A. D. Caplin, Phys. Rev. B **56**, 2809 (1997).
[18] D. Karmakar and K. V. Bhagwat, Phys. Rev. B **65**, 024518 (2001).
[19] G. P. Mikitik and E. H. Brandt, Phys. Rev. B **62**, 6800 (2000).
[20] E. H. Brandt, Phys. Rev. B **54**, 4246 (1996).
[21] E. H. Brandt, Phys. Rev. B **64**, 024505 (2001).
[22] M. R. Koblischka and R. J. Wijngaarden, Supercond. Sci. Technol. **8**, 199 (1995).
[23] R. J. Wijngaarden, K. Heeck, M. Welling, R. Limburg, M. Pannetier, K. van Zetten, V. L. G. Roorda, and A. R. Voorwinden, Rev. Sci. Instrum. **72**, 2661 (2001).
[24] R. J. Wijngaarden, C. M. Aegerter, M. S. Welling, and K. Heeck, *Magneto-optical Imaging, NATO SCIENCE SERIES: II: Mathematics, Physics and Chemistry: Volume 142*, edited by T. H. Johansen and D. V. Shantsev (Kluwer Academic, Dordrecht, 2003), p. 61.
[25] W. Goldacker, R. Ahrens, M. Nindel, B. Obst, and C. Meingast, IEEE Trans. Appl. Supercond. **3**, 1322 (1993).
[26] E. H. Brandt, Rep. Prog. Phys. **58**, 1465 (1995).
[27] R. J. Wijngaarden, H. J. W. Spoelder, R. Surdeanu, and R. Griessen, Phys. Rev. B **54**, 6742 (1996).
[28] R. J. Wijngaarden, K. Heeck, H. J. W. Spoelder, R. Surdeanu, and R. Griessen, Physica C **295**, 177 (1997).
[29] T. H. Johansen, M. Baziljevich, H. Bratsberg, Y. Galperin, P. E. Lindelof, Y. Shen, and P. Vase, Phys. Rev. B **54**, 16264 (1996).
[30] F. Laviano, D. Botta, A. Chiodoni, R. Gerbaldo, G. Ghigo, L. Gozzelino, S. Zannella, and E. Mezzetti, Supercond. Sci. Technol. **16**, 71 (2003).
[31] R. Surdeanu, R. J. Wijngaarden, E. Visser, J. M. Huijbregtse, J. H. Rector, B. Dam, and R. Griessen, Phys. Rev. Lett. **83**, 2054 (1999).